GSI

Preprint 2003 - 21
July

# Exclusive measurement of breakup reactions with the one-neutron halo nucleus $^{11}$Be

R. Palit, P. Adrich, T. Aumann, K. Boretzky, B. V. Carlson, D. Cortina, Th. W. Elze, H. Emling, H. Geissel, M. Hellström, K. L. Jones, J. V. Kratz, R. Kulessa, Y. Leifels, A. Leistenschneider, G. Münzenberg, C. Nociforo, P. Reiter, H. Simon, K. Sümmerer, W. Walus (LAND/FRS coll.)

(Submitted to Physical Review C)

Gesellschaft für Schwerionenforschung mbH
Planckstraße 1 • D-64291 Darmstadt • Germany
Postfach 11 05 52 • D-64220 Darmstadt • Germany

# Exclusive measurement of breakup reactions with the one-neutron halo nucleus $^{11}$Be

R. Palit,[1] P. Adrich,[2,3] T. Aumann,[3,*] K. Boretzky,[4] B.V. Carlson,[5] D. Cortina,[3] Th.W. Elze,[1] H. Emling,[3] H. Geissel,[3] M. Hellström,[3] K.L. Jones,[3] J.V. Kratz,[4] R. Kulessa,[2] Y. Leifels,[3] A. Leistenschneider,[1] G. Münzenberg,[3] C. Nociforo,[4] P. Reiter,[6] H. Simon,[3,7] K. Sümmerer,[3] and W. Walus[2] (LAND/FRS collaboration)[†]

[1] *Institut für Kernphysik, Johann Wolfgang Goethe Universität, D-60486 Frankfurt, Germany*
[2] *Instytut Fizyki, Uniwersytet Jagelloński, PL-30-059 Kraków, Poland*
[3] *Gesellschaft für Schwerionenforschung (GSI), Planckstr. 1, D-64291 Darmstadt, Germany*
[4] *Institut für Kernchemie, Johannes Gutenberg Universität, D-55099 Mainz, Germany*
[5] *Instituto Tecnologico de Aeronautica, CTA, Sao Jose dos Campos, Brazil*
[6] *Institut für Kernphysik, Universität Köln, D-50937 Köln, Germany*
[7] *Institut für Kernphysik, Technische Universität Darmstadt, D-64289 Darmstadt, Germany*

(Dated: 08-07-03)

Electromagnetic and nuclear inelastic scattering of the halo nucleus $^{11}$Be have been investigated by a measurement of the one-neutron removal channel, utilizing a secondary $^{11}$Be beam with an energy of 520 MeV/nucleon impinging on lead and carbon targets. All decay products, i.e. $^{10}$Be fragments, neutrons, and gamma-rays have been detected in coincidence. Partial cross sections for the population of ground and excited states in $^{10}$Be were determined for nuclear diffractive breakup as well as for electromagnetically induced breakup. The partial cross sections for ground-state transitions have been differentiated further with respect to excitation energy, and the dipole-strength function associated solely with transitions of the halo $2s_{1/2}$ neutron to the continuum has been derived. The extracted dipole strength integrated from the neutron threshold up to 6.1 MeV excitation energy amounts to 0.90(6) $e^2$fm$^2$. A spectroscopic factor for the $\nu 2s_{1/2} \otimes ^{10}$Be($0^+$) single-particle configuration of 0.61(5) and a root-mean-square radius of the $2s_{1/2}$ neutron wave function of 5.7(4) fm have been deduced.

PACS numbers: 21.10.Jx, 21.10.Gv, 24.50.+g, 25.60Gc

## I. INTRODUCTION

The investigation of nuclei near the drip lines via breakup reactions at intermediate and high energies has attracted significant interest in the past decade due to the availability of fast radioactive beams produced by in-flight fragmentation [1]. Such relatively high beam energies (ranging from about 50 MeV/nucleon to 1 GeV/nucleon) are advantageous both from an experimental point of view as well as from theoretical considerations. The high beam energies result in short interaction times and small scattering angles, which allow the use of certain approximations and thus a quantitative description of the underlying reaction mechanisms. Experimental merits are the possibility of using relatively thick targets (in the order of g/cm$^2$) and kinematical forward focusing, which makes full-acceptance measurements feasible with moderately sized detectors. Thus nuclear-structure investigations of very exotic nuclei at the drip lines are possible even if such beams are produced with very low rates in the order of one ion per second.

Depending on their intrinsic structure, some of these weakly bound atomic nuclei show the interesting property of a very large spatial extension compared to its near neighbors [2–5]. Such a halo-like low-density tail of the neutron wave function has a definite impact on the observables in breakup reactions. These are for example the large cross sections and narrow momentum distributions observed in the nuclear one-neutron removal channel. Recently, semi-exclusive experiments of this kind were performed and quantitative information on the single-particle structure like spin assignments and spectroscopic factors were obtained. We refer to Ref. [6] for a recent review and to Ref. [7] for the case of the one-neutron halo nucleus $^{11}$Be, which is the object of interest here. Two processes are considered to be important for the nuclear one-neutron removal channel: i) Knockout of one nucleon by a (quasi-free) nucleon-target reaction, and ii) inelastic excitation into the continuum or diffractive dissociation. So far, experiments have not differentiated the two contributions and have deduced nuclear-structure information by comparing the experimental cross section with the sum of the calculated cross sections for the two mechanisms by using an Eikonal model. The fact that the two reaction mechanisms result in very different neutron-fragment relative momentum domains has been exploited in the present experiment to separate the two contributions.

Another important subject of the paper deals with a complementary process, the one-neutron removal induced by the electromagnetic interaction. Here, the projectile is excited into the continuum by absorbing a vir-

*Electronic address: t.aumann@gsi.de
†URL: www-land.gsi.de

tual photon generated by the rapidly changing electromagnetic field of a target with high nuclear charge. The large radial extension of the neutron density distribution of halo nuclei results in large non-resonant dipole-transition probabilities close to the neutron threshold. This 'threshold strength' was observed experimentally for several halo nuclei, e.g. for the two-neutron halo nuclei $^{6}$He [8] and $^{11}$Li [9–11], and for the one-neutron halo nuclei $^{11}$Be [12, 13] and $^{19}$C [14]. The phenomenon is theoretically well understood [15–18]. The shape of the excitation-energy differential cross section is thereby directly related to the wave function of the loosely bound valence nucleon of the projectile [12, 14, 19], and the root-mean-square (rms) radius of the neutron density distribution may be extracted from the sum-rule exhaustion [8]. First exclusive experiments involving fragment-neutron-gamma triple coincidences were performed only very recently for the more tightly bound neutron-rich carbon isotopes $^{15}$C and $^{17}$C [19], demonstrating this method to be a sensitive spectroscopic tool. In the present paper, we discuss the results of an exclusive measurement of the electromagnetic dissociation of the halo-nucleus $^{11}$Be. The coincident measurement of gamma rays allowed for the first time to extract the partial differential cross section related solely to the halo-neutron density, i.e. for the $\nu 2s_{1/2}\otimes^{10}\mathrm{Be}(0^+)$ single-particle configuration, providing a spectroscopic factor and the rms radius.

The question arises how precise are spectroscopic factors deduced from reactions with secondary beams. So far, mainly reactions involving the nuclear interaction have been employed, in particular the one-nucleon removal reaction [6]. Recently, a first experiment has been performed investigating the transfer reaction in inverse kinematics [20, 21]. In case of $^{11}$Be, spectroscopic factors have been obtained ranging from 0.4 to 0.8 for the $\nu 2s_{1/2}\otimes^{10}\mathrm{Be}(0^+)$ configuration. Two major uncertainties arise in the case of transfer reactions with $^{11}$Be: the parameters of the optical potentials used [21, 22], and the difficulties in the description of the reaction theory [22]. The analysis of transfer data from Ref. [23] with an elaborated reaction model including excitations and breakup of the halo nucleus as well as the deuteron results in spectroscopic factors as low as 0.36 for the halo configuration [22], much in contrast to the result obtained from the neutron-removal reaction [7] which was found to be in agreement with the shell-model prediction of Warburton and Brown [24, 25] of 0.74. The shell model predicts also correctly the parity inversion of the $^{11}$Be ground state, i.e. the correct ordering for the $2s_{1/2}$ and $1p_{1/2}$ levels. This level inversion is manifested also in the vanishing of the $N = 8$ shell closure [26, 27]. Although the shell-model calculations provide a fully anti-symmetrized wave function, the harmonic oscillator expansions usually used are not adequate to describe the halo states. Effective charges, pairing interactions and coupling to the continuum are all necessary corrections to the shell model [28, 29]. The fact that the electromagnetic interaction is well understood and that a quantitative description of the excitation process with relativistic heavy ions is available [30–32] and established for stable nuclei [33] suggests possible advantages of utilizing this reaction mechanism for nuclear-structure studies of exotic nuclei and may shed light on the problem sketched above. Remaining uncertainties and dependencies on the parameters used in the reaction-model description are discussed in the paper.

We have organized the paper in the following way. Section II describes the experimental set-up and details of the detection scheme. In section III, the results are described and compared with model calculations for nuclear (III B) and Coulomb breakup (III C). The conclusions are summarized in IV.

## II. EXPERIMENTAL METHOD

The experimental method consists of producing high-energy radioactive beams and a kinematical measurement of breakup products in secondary targets, allowing the reconstruction of the excitation energy by utilizing the invariant-mass method. The measurement is exclusive or kinematically complete in the sense that all projectile-like decay products are detected, i.e. reaction products with velocities close to the beam velocity. Target-like reaction products are not measured (with the exception of $\gamma$-rays). A schematic drawing of the detection setup is shown in Figure 1. Details of the experiment are described in the following.

The secondary beam containing $^{11}$Be ions with a kinetic energy of 520 MeV/nucleon was produced in fragmentation reactions of a primary $^{40}$Ar beam delivered by the heavy-ion synchrotron SIS at GSI, Darmstadt. The 720 MeV/nucleon $^{40}$Ar beam with an intensity of about $10^{10}$ ions per second impinged on a beryllium production target of 5 g/cm$^2$ thickness. Fragments were selected according to magnetic rigidity by the Fragment Separator (FRS) [34] and then transported to the experimental area. The settings of the magnetic fields of the FRS and the beam-transport line were optimized for the transmission of $^{22}$O ions [35, 36]. Except for two thin plastic scintillation detectors at the middle focal plane of the separator and at an intermediate focus in the beam-transport line, no additional degrader was inserted in order to produce a 'mixed' secondary beam containing various isotopes. Corresponding to the selected magnetic rigidity, isotopes with similar mass-to-charge ratio $A/Z$ were transmitted, ranging from beryllium to fluorine with $A/Z$ from 2.4 to 2.8. Beam ions incident on the secondary target (0.573 g/cm$^2$ $^{\mathrm{nat}}$C or 1.820 g/cm$^2$ $^{\mathrm{nat}}$Pb) were identified uniquely on an event-by-event basis: The nuclear charge $Z$ was obtained from an energy-loss measurement in a Si pin-diode placed about 80 cm in front of the target (position 2 in Figure 1); the mass-to-charge ratio was obtained from a time-of-flight measurement using thin organic scintillators, one placed at an intermediate focus in the beam-transport line and the second one about 85 m downstream close to the target (position 2

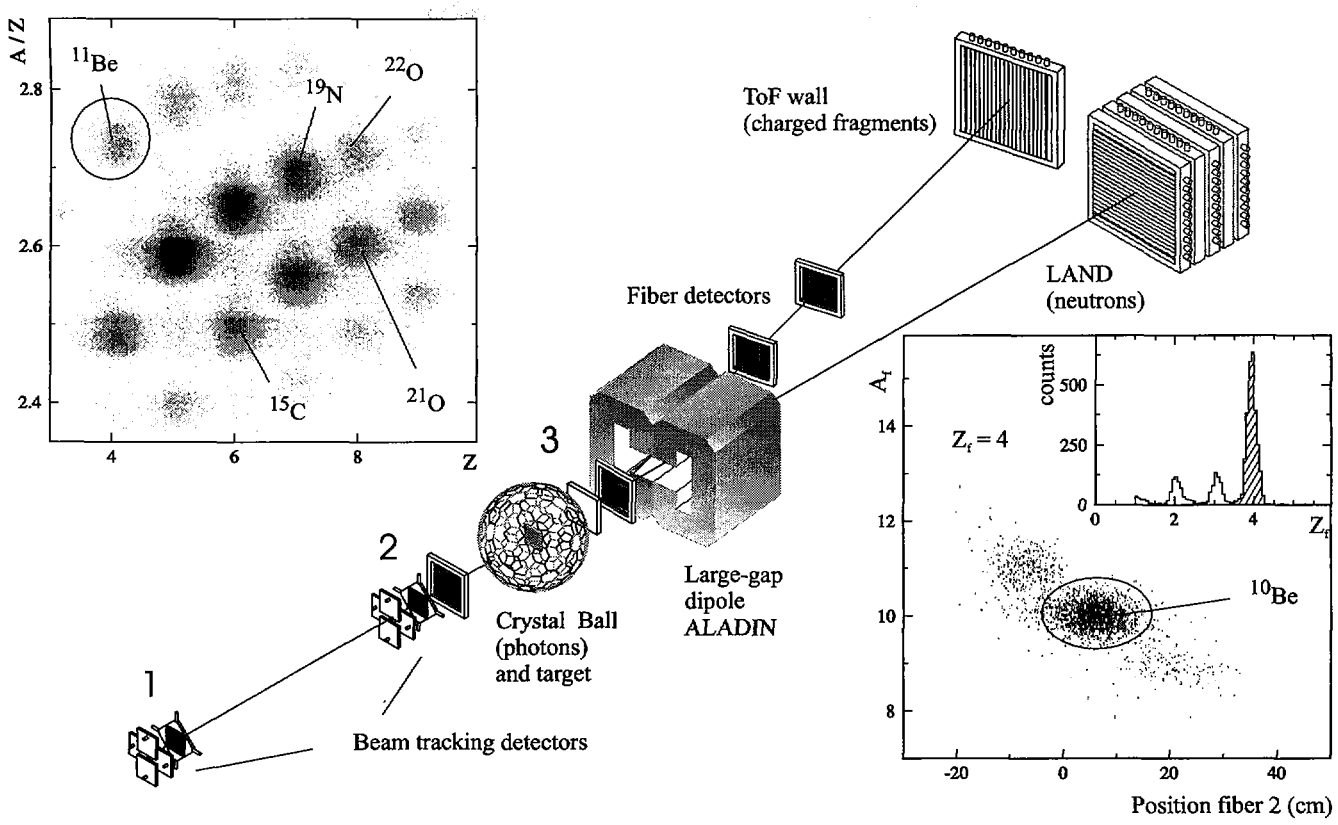


FIG. 1: Schematic drawing of the detection setup (not scalable). Shown are the beam and fragment detectors (see text), the Crystal Ball photon spectrometer, the dipole magnet ALADIN, and the neutron detector LAND. The upper left insert shows the composition of the mixed radioactive beam impinging onto the secondary targets, which are inserted at the center of the Crystal Ball. The lower right insert displays the fragment identification for reactions of $^{11}$Be on a lead target.

in Fig. 1). The upper left insert in Figure 1 shows the composition of the beam identified as described above. The intensity of the $^{11}$Be beam amounted typically to about 20 ions per second, the accumulated statistics for breakup on the lead target corresponds to about one and a half day of data taking.

The emittance of the secondary beam was defined by two active collimators limiting the beam-spot size on the target to $25 \times 25$ mm$^2$. One was placed at the entrance of the experimental area (position 1 in Fig. 1) with a diameter of 6 cm, the second one was placed 11 m downstream close to the target (position 2 in Fig. 1) The position of the incoming particles on the target was measured by a position-sensitive Si pin-diode (position 2 in Fig. 1) with a resolution of $\sigma_{x,y} = 2.3$ mm. The nuclear charge $Z_f$ and the scattering angles of the outgoing fragments were determined by energy-loss and position measurements utilizing $45 \times 45$ mm$^2$ sized Si pin-diodes placed about 80 cm behind the secondary target (position 3 in Fig. 1). The overall resolution for the determination of the scattering angle amounted to $\sigma_\vartheta = 6$ mrad including the multiple scattering in the lead target. In order to detect the $\gamma$-rays emitted from excited $^{10}$Be fragments, the target was surrounded by the $4\pi$- Crystal Ball spectrometer, consisting of 160 NaI detectors [37]. The granularity of the detector allows the determination of the $\gamma$-emission angle, which is used to reconstruct the energy of the photon in the rest frame of the emitting source on an event-by-event basis. The resolution ($\sigma$) obtained for the corrected energy of 10% at 3.3 MeV was dominated by the Doppler broadening resulting from the determination of the emission angle.

Behind the target, the fragments were deflected by a large-gap dipole magnet (ALADIN). The trajectories of the fragments in the magnetic dipole field was determined by three position measurements in the dispersive plane ($x$), one before the magnet using a position-sensitive Si pin-diode and two times behind the magnetic field by large-area ($50 \times 50$ cm$^2$) fiber detectors [38] with a pitch of 1 mm and with a distance of about 2 m between each other. The deflection angle in the dipole field, and thus the magnetic rigidity $B\rho$ is determined by these three position measurements. Finally, the velocity was determined via a time-of-flight measurement between a thin organic plastic scintillator placed close to the target (see above) and an array of 20 organic scintillators (ToF wall) with an active area of $2 \times 2$ m$^2$ and 5 mm thickness placed about 13 m downstream from the target (resolution $\sigma_{\mathrm{ToF}} = 250$ ps). The acceptance for the $^{10}$Be fragments amounted to 100%. The nuclear charge $Z_f$ of the

fragments was determined by combining the energy-loss measurements in the Si-pin diode behind the target and the energy-loss information from the ToF wall, while the fragment mass $A_f$ can be deduced from the $B\rho$ determination by applying the relation $B\rho \sim A/Z\beta\gamma$, $\beta$ and $\gamma$ denoting the velocity $v/c$ and the relativistic Lorentz factor, respectively. An example for the fragment identification behind the target according to charge $Z_f$ and mass $A_f$ is shown in the lower right panel of Figure 1 for the breakup of $^{11}$Be on a lead target. Since the one-neutron removal is by far the dominating channel, the intensity is shown on a logarithmic scale.

The neutrons stemming from the decay of the excited projectile or from excited projectile-like fragments are kinematically focussed into the forward direction and were detected with high efficiency in the LAND neutron detector [39]. The detector has an active area of $2 \times 2$ m$^2$ and was placed about 11 m downstream from the target at 0 degrees, thus covering horizontal and vertical angular ranges of about $\pm 80$ mrad. This angular range is sufficient to provide a 100% acceptance for neutrons emitted from the projectile with kinetic energies up to 5.6 MeV in the transverse direction. The detector consists of 200 individual modules ($2 \times 0.1 \times 0.1$ m$^3$) allowing multi-hit recognition, which was, however, not necessary in the present experiment. These individual 10 cm thick detector modules have a sandwich-like structure (alternating layers of 5 mm iron converter and 5 mm plastic scintillator) and are read out from the two far-end sides providing time-of-flight (from the mean time, resolution $\sigma_{\mathrm{ToF}} = 250$ ps) and position (from the time difference, resolution 7 cm FWHM) information. The position resolution in the second transverse and the longitudinal directions are determined by the size (10 cm) of the modules. The total thickness of the detector of 1 m (50% iron, 50% plastic) provides a detection efficiency of 94% for one single neutron with kinetic energies around 500 MeV.

By measuring the four-momenta $\boldsymbol{P}_i$ of all products of the decaying system as described above, the excitation energy $E^*$ of the nucleus prior to decay can be reconstructed on an event-by-event basis by analyzing the invariant mass $M$,

$$M^2c^2 = \left(\sum_i \boldsymbol{P}_i\right)^2 = (m_pc^2 + E^*)^2/c^2, \qquad (1)$$

where $m_p$ denotes the projectile rest mass. The energy $E_\gamma$ released by $\gamma$-rays (in the projectile rest frame) can be separated to good approximation and the above equation can be rewritten for the one-neutron decay channel, so that the excitation energy $E^*$ is given by

$$E^* = \left(m_n^2c^2 + m_f^2c^2 + 2E_nE_f(1 - \beta_n\beta_f\cos(\vartheta_{nf})\right)^{1/2} - m_pc^2 + E_\gamma, \qquad (2)$$

with $m_{n(f)}$, $E_{n(f)}$, and $\beta_{n(f)}$ denoting the ground-state rest mass, the total energy, and the velocity $v/c$ of the neutron (fragment), respectively. $\vartheta_{nf}$ represents the relative angle between neutron and fragment in the laboratory frame. In case of decay to the ground state of the fragment, the excitation energy relates to the relative kinetic energy as $E_{rel} = E^* - B_n$ between the fragment and the neutron, where $B_n$ is the neutron separation energy, $B_n = 507$ keV for $^{11}$Be.

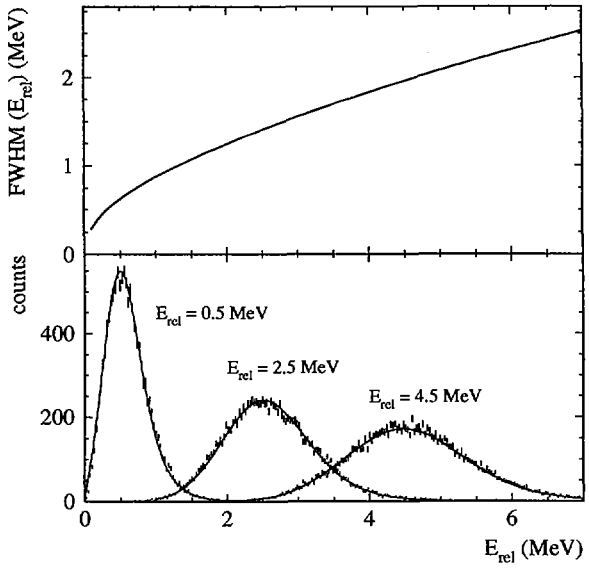


FIG. 2: The upper frame shows the overall resolution (FWHM) with regard to the relative energy between $^{10}$Be and the neutron after the decay of $^{11}$Be as a function of relativ energy $E_{rel}$. The energy response of the experimental setup is shown in the lower panel for three relative energies of $E_{rel} = 0.5$ MeV, 2.5 MeV, and 4.5 MeV, respectively.

The acceptance of the experimental setup for the coincident detection of a $^{10}$Be fragment and a neutron was obtained from Monte-Carlo event simulations. Up to relative energies of $E_{rel} = 5.6$ MeV between fragment and neutron, the efficiency and acceptance is constant (94%) and then decreases continuously to about 25% at $E_{rel} = 15$ MeV due to acceptance losses for the neutron in the transverse directions (see above). However, all differential cross sections (with respect to excitation-energy) given in the following correspond to the relative-energy region with an acceptance of 100% for the coincident detection of neutron and fragment. Thus, no acceptance correction was necessary for the cross sections up to 6.1 MeV excitation energy. The overall resolution FWHM($E_{rel}$) with regard to the relative energy between $^{10}$Be and the neutron after the decay of $^{11}$Be is depicted in Fig. 2. It changes from about 250 keV close to the threshold to about 2 MeV around $E_{rel} = 5$ MeV. The instrumental response as obtained from the Monte-Carlo simulation is given in the lower part of Fig. 2 for three different relative energies. Prior to comparison with the data, the theoretical cross sections were convoluted with a response matrix derived from such simulated spectra. [72]

## III. EXPERIMENTAL RESULTS AND DISCUSSION

### A. Reaction mechanisms and cross sections

The present scattering experiment focuses on an exclusive measurement of the one-neutron removal reaction on carbon and lead targets. In the former case, the reaction is dominated by the nuclear interaction, while in the latter case the electromagnetic interaction will dominate the process. Thereby, not only the valence or halo neutron can be removed in the reaction, but also more deeply bound neutrons might be removed from an inner shell, i.e. from a core state. Commonly, three different reaction mechanisms are considered to contribute to the one-neutron removal channel:

i) **Electromagnetic dissociation** or **Coulomb breakup** due to the rapidly varying electromagnetic field of a high-Z target experienced by the fast moving projectile. The inelastic electromagnetic scattering may populate resonant states (e.g. the giant dipole resonance), or cause non-resonant transitions into the continuum. The latter process is especially important for weakly bound nucleons yielding large dipole-transition matrix elements close to the neutron threshold ('threshold strength'). Due to the smaller effective charge for higher multipolarities [40], the cross section is dominated by dipole excitations.

ii) **Nuclear inelastic scattering** into the resonant or non-resonant continuum. In case of halo nuclei, this process is often considered as a diffractive dissociation or **diffraction** of the neutron, analogous to Fraunhofer diffractive scattering of light on a black sphere. Since this process corresponds to an elastic scattering of the neutron off the target, this reaction mechanism is frequently referred to as **elastic breakup**.

iii) **Knockout** of a neutron from the projectile or **inelastic breakup**. The knockout reaction may be viewed as a quasi-free (inelastic) scattering of the neutron off the target. The neutron-target reaction will result in a relatively large momentum transfer to the neutron. As a consequence, the neutron will be scattered to large angles or even be absorbed by the target and will thus not appear as a projectile-like fragment in the forward direction (with a velocity close to the beam velocity). In the literature, this process is sometimes referred to as **absorption** or **stripping**.

Since the present experiment detects coincidences between the $^{10}$Be fragment and one neutron in the forward direction (see section II), only inelastic excitations of the projectile, i.e. the processes i) and ii), contribute to the measured cross section. (The probability to detect a neutron from a knockout process in the angular range covered by the LAND was estimated in Ref. [11] to be negligible.) This is different from the semi-exclusive measurements of one-neutron removal reactions (see e.g. [7]), where both knockout and diffraction contribute. Differential cross sections $d\sigma/dE^*$ were measured for carbon and lead targets by applying the invariant-mass method (see section II, equation 2). An additional measurement without target was performed in order to determine background from non-target interactions, which was subtracted after proper normalization from the measurement with target. Such background contributions amounted to 25% and 6% for the measurements with carbon and lead targets, respectively. The resulting total $1n$-removal cross sections, integrated up to neutron-fragment relative energies of 5.6 MeV, are given in the last row of Table I for the two targets used. The large increase of the cross section by about a factor of 20 for the lead target compared to the carbon target indicates the dominance of electromagnetically induced breakup in case of the heavy target.

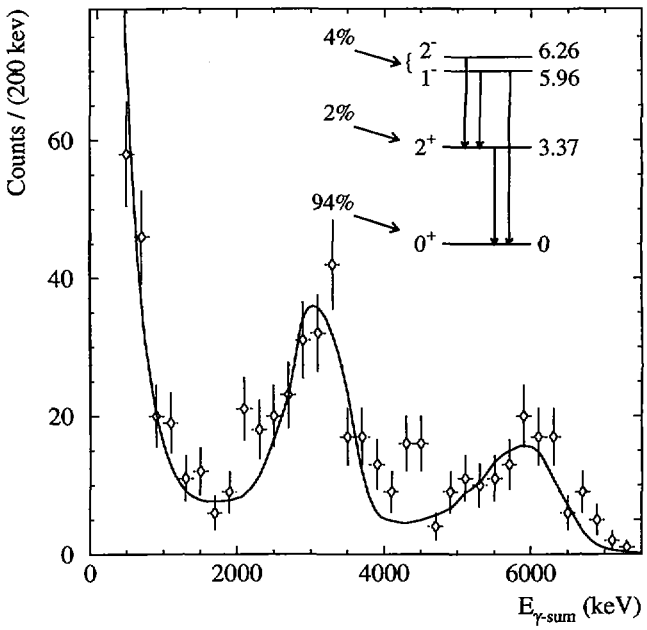


FIG. 3: Doppler corrected $\gamma$-sum energy spectrum measured with the Crystal Ball in coincidence with a $^{10}$Be fragment and a neutron for the lead target. The solid curve is a fit to the experimental spectrum using response functions generated by GEANT Monte-Carlo simulations. The insert shows a partial level scheme for $^{10}$Be [41] indicating the observed transitions and the population after breakup. The energy of the levels is given in MeV.

The cross sections are experimentally further differentiated according to the $^{10}$Be states populated by analyzing the coincident $\gamma$-decay transitions of the core fragments. Since the Crystal-Ball spectrometer covers the full solid angle, the $\gamma$-ray sum energy can be determined reflecting directly the excitation energy of the excited

TABLE I: Partial cross sections (integrated up to $E_{rel} = 5.6$ MeV) for breakup of $^{11}$Be on Pb and C targets populating different states $I^\pi$ of $^{10}$Be. For the lead target, the electromagnetic (EM) contribution is given in addition. The calculated single-particle cross sections for diffraction ($\sigma_{sp}^{diff}$) and electromagnetic breakup ($\sigma_{sp}^{EM}$) are also given. The spectroscopic factors $C^2S$ are given in the last two columns.

| | $\sigma_{Expt}$ (mb) | | | $\sigma_{Calculated}$ (mb) | | | | | |
|---|---|---|---|---|---|---|---|---|---|
| | C-target | Pb-target | | C-target | | Pb-target | | $C^2S$ | |
| $I^\pi$ | | tot | EM | $\sigma_{sp}^{diff}$ | $\sigma_{sp}^{EM}$ | $\sigma_{sp}^{diff}$ | $\sigma_{sp}^{EM}$ | Expt | shell model[c] |
| $0^+$ | 26.9(1.4) | 605(30) | 477(32) | 29.8 | 5.3 | 160 | 786 | 0.77(4)[a], 0.61(5)[b] | 0.74 |
| $2^+$ | 2.2(6) | 13(3) | 7.6(3.3) | 6.6 | | 16.2 | | | 0.18 |
| $1^-$ | 2.3(6) | 13(2) | 7.5(2.5) | 5.2 | | 12.4 | | | 0.69 |
| $2^-$ | 1.2(6) | 12(3) | 9.1(3.3) | 5.0 | | 11.9 | | | 0.58 |
| $\Sigma$ | 32.6(1.6) | 643(32) | 501(32) | | | | | | |

[a]Evaluated from diffraction cross section.
[b]Evaluated from Coulomb breakup.
[c]Shell-model predictions of Brown *et al.* [7, 25]

state. Figure 3 shows the Doppler-corrected $\gamma$-sum energy spectrum as measured in coincidence with one neutron and a $^{10}$Be fragment in case of the lead target. The spectrum shows the first excited $2^+$ state at 3.37 MeV and also higher lying states of $^{10}$Be at around 6 MeV excitation energy. The response functions corresponding to the individual $\gamma$-rays were generated with the Monte-Carlo code GEANT [42] in a simulation procedure that took into account the Doppler shift. The low-energy (below $\approx 1$ MeV) background originates from atomic interactions of the beam with the lead target, mainly due to Bremsstrahlung generated by fast electrons. The shape of this low-energy background was obtained from the gamma spectrum in coincidence with the non-interacting beam. The calculated line shapes, together with this background give the fit to the measured spectrum shown as the solid curve. The intensities of the different gamma lines were obtained from this fit; the transitions which were considered are indicated in the partial level-scheme [41] shown as the insert in Figure 3. The partial cross sections populating the individual excited states are extracted from these intensities taking into account the detection efficiency as derived from the simulation. The resulting partial cross sections for breakup of $^{11}$Be populating the different states of $^{10}$Be are given in Table I for lead and carbon targets. Clearly, the dominant contribution to the cross sections stems from ground-state transitions, i.e. from the removal of the $2s_{1/2}$ halo neutron, which amounts to 83% and 94% for carbon and lead, respectively. The differential cross sections with respect to excitation energy $E^*$ (see equation 2) are shown in Figure 4 for ground-state transitions. Excited-state contributions as obtained from the coincidences with $\gamma$-transitions were subtracted from the total cross section. These differential cross sections can thus be solely associated to excitations of the $s_{1/2}$ halo neutron.

The shapes of the excitation spectra observed for the carbon (upper frame in Fig. 4) and lead target (lower frame) are very different reflecting the different excitation mechanisms, i.e. nuclear and electromagnetic excitations. This fact can be used to independently extract the nuclear contribution to the cross section for the lead target (see also the following subsections). The solid curve in Fig. 4 displays the sum of the calculated cross section for electromagnetic excitation of the $2s_{1/2}$ neutron (see below) and an assumed nuclear contribution taken from the measurement with the carbon target. The normalization of the calculation as well as the scaling factor for the nuclear cross section were determined in a $\chi^2$-minimization procedure. The fit results in a ratio $\sigma(\mathrm{Pb})/\sigma(\mathrm{C})$ for the nuclear diffraction cross sections (exclusively for the $s_{1/2}$ halo neutron) of 5.6(4), much larger than expected from a geometrical scaling for peripheral reactions with the target radius ($\approx 2.6$), but in good agreement with the expectation from an Eikonal calculation (see below). In the following two subsections, the nuclear and Coulomb breakup will be discussed in more detail after recalling briefly the underlying reaction theory as far as it is important for the discussion.

### B. Nuclear breakup

The cross sections for the nuclear induced one-neutron removal reaction can be calculated using the Eikonal approximation, which is well justified at the high beam energy of 520 MeV/nucleon used here. The single-particle cross sections $\sigma_{\mathrm{sp}}^{\mathrm{diff}}$ and $\sigma_{\mathrm{sp}}^{\mathrm{knock}}$ for the two contributing reaction mechanisms, diffraction and knockout, respectively, can be calculated separately [43, 44]:

$$\sigma_{\mathrm{sp}}^{\mathrm{diff}} = \int d\boldsymbol{b}\, [\langle|(1 - S_c S_n)|^2\rangle - |\langle(1 - S_c S_n)\rangle|^2], \quad (3)$$

$$\sigma_{\mathrm{sp}}^{\mathrm{knock}} = \int d\boldsymbol{b}\, \langle(1 - |S_n|^2)|S_c|^2\rangle. \quad (4)$$

Here, $\langle\ \rangle$ denotes a ground-state expectation value and $S_c$ and $S_n$ the profile functions for the core-target and

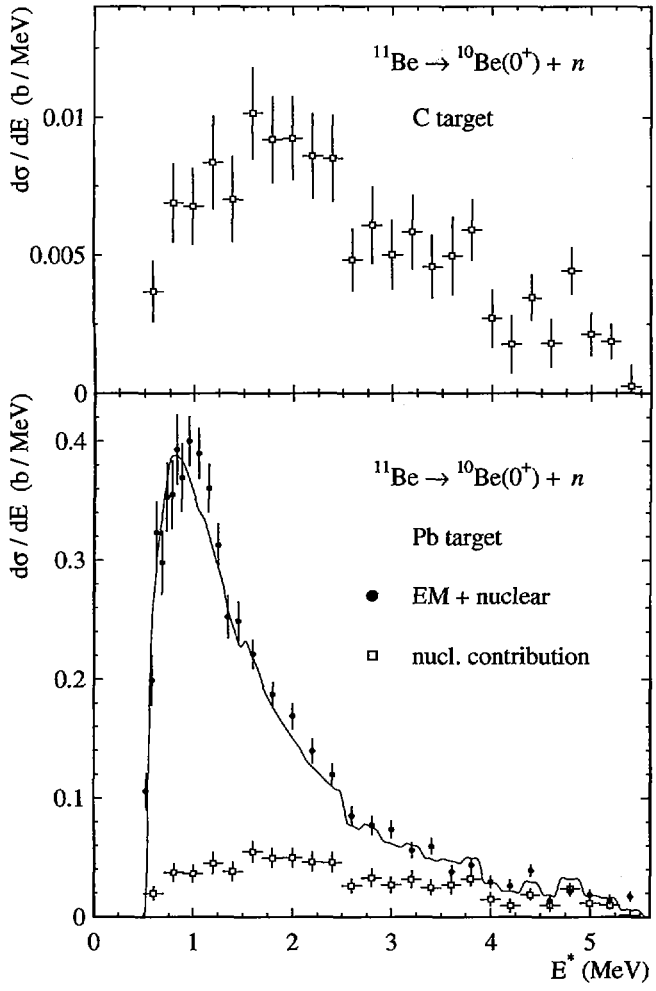


FIG. 4: Differential cross sections with regard to excitation energy $E^*$ for the reaction 520 MeV/nucleon $^{11}$Be + C,Pb → $^{10}$Be(0$^+$) + $n$ for carbon (upper frame) and lead (lower frame) targets. Contributions populating excited states of $^{10}$Be are subtracted. The solid curve displays the sum of the nuclear contribution (open symbols) as obtained from the measurement with carbon target and a theoretical cross section for the electromagnetic dipole excitations. The normalization of the two contributions was obtained by a fit to the experimental data.

neutron-target systems, respectively. The quantities $S_c$ and $S_n$ are expressed as functions of their individual impact parameters and are calculated in the Eikonal approximation using density distributions for the target and the core with parameters reproducing measured cross sections. For the $^{12}$C target, a harmonic oscillator density distribution [45] with parameters $a = 1.60$ and $\alpha = 1.026$ is used, which reproduces the empirical rms radius of 2.32 fm [3], the reaction cross section for $^{12}$C + $^{12}$C of 856(9) mb [46] measured at 790 MeV/nucleon, and the neutron plus $^{12}$C reaction cross section of 209(22) mb [47] within their experimental errors. For the core, the density distribution of the $^{10}$Be ground state is adopted. With the parameters $a = 1.65$ and $\alpha = 0.588$ for the harmonic oscillator density the interaction cross section for 790 MeV/nucleon $^{10}$Be + $^{12}$C of 813(10) mb [2] is reproduced. For the lead target, a two-parameter Fermi distribution [45] is used with parameters $c = 6.53$ and $z = 0.546$ reproducing $n$+$^{208}$Pb cross sections at 549 MeV and 860 MeV [47]. In addition, only free nucleon-nucleon cross sections at 520 MeV/nucleon [48] enter the calculation; no real optical potential is needed at these high energies [43] (see also Table 2.2 in Ref. [17] and Ref. [49]). As an approximation, we make use of the 'no recoil limit' [44], in which the impact parameter of the core is assumed to coincide with the impact parameter **b** of the projectile. In this case the core-target profile function can be taken outside the expectation value and the probability, e.g., for the one-neutron knockout, reduces to

$$\begin{aligned} P(\boldsymbol{b}) &= S_c^2(\boldsymbol{b})\langle 1 - S_n^2(\boldsymbol{b}_n)\rangle \\ &= S_c^2(\boldsymbol{b}) \int d^3r \; |\phi_{nlj}(\boldsymbol{r})|^2 (1 - S_n^2(\boldsymbol{b}_n)), \end{aligned} \quad (5)$$

where $\phi_{nlj}(\boldsymbol{r})$ denotes the single-particle wave function with quantum numbers $nlj$ expressed in terms of the relative core-neutron distance $\boldsymbol{r}$. In this representation, $S_n$ and $S_c$ have a very clear meaning: $\langle 1 - S_n^2 \rangle$ yields the reaction probability of the neutron with the target, while $S_c$ guaranties the survival of the core ('shadowing effect'). The result is a surface-peaked reaction probability as displayed in Figure 5 (dash-dotted curve) for the knockout of the $2s_{1/2}$ neutron from $^{11}$Be on a lead target. A similar equation is obtained for the diffractive breakup. The total probability for a nuclear reaction of $^{11}$Be with the target is shown as a function of impact parameter by the dashed curve. The neutron-core relative-motion wave functions $\phi_{nlj}$ are calculated in a Woods-Saxon potential with radius $r_0 = 1.25$ fm and diffuseness $a = 0.7$ fm. The theoretical cross section is calculated separately for the removal of a neutron with angular momentum $l$ coupled to a core state $I^\pi$ with separation energy $B_n$, and is commonly assumed to be a product of a spectroscopic factor $C^2S$ and a single-particle cross section given by the sum of equations 3 and 4 [50]. The total (inclusive) one-neutron removal cross section can be evaluated by summing over all contributing configurations.

At high beam energies the one-neutron removal cross section is dominated by knock-out, and a small flux goes to diffraction as reported in Ref. [43], while at lower energies, e.g., at 60 MeV/nucleon, the two contributions are of similar size. The experimental total cross section for inelastic excitations of $^{11}$Be on carbon target yielding $^{10}$Be and a neutron in the final state is obtained by integrating the inclusive (without condition on $\gamma$-rays) invariant mass spectrum. For an integration limit of 5.6 MeV for the relative energy (up to which no acceptance correction is necessary), we obtain a cross section of 32.6(1.6) mb, where the major part, 26.9(1.4) mb, yields the core in its ground state. This can be compared to 29.8 mb resulting from equation 3 for the diffraction

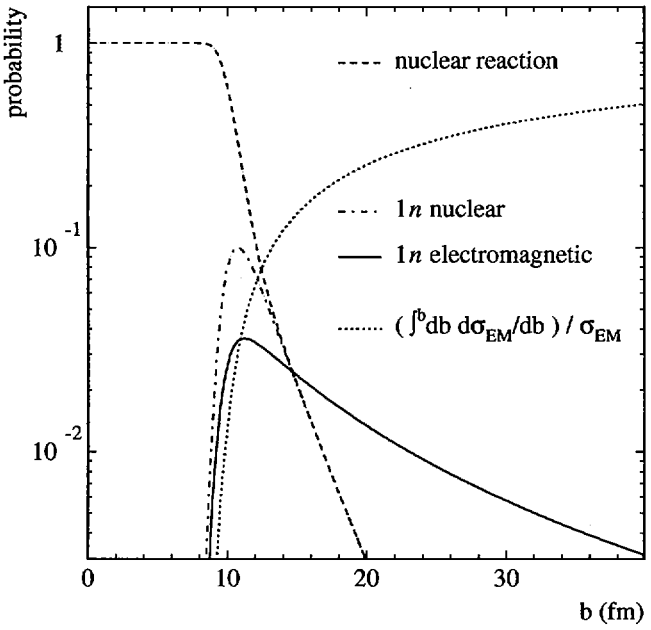


FIG. 5: Dissociation probabilities for 520 MeV/nucleon $^{11}$Be on lead as a function of impact parameter $b$. The dashed curve displays the total nuclear reaction probability, while the dash-dotted and solid curves show the one-neutron removal probability for nuclear and electromagnetic dissociation, respectively. The dotted curve indicates the cross section for electromagnetic dissociation as a function of the upper integration limit b, normalized to its asymptotic value. This value reaches 50% for $b = 40$ fm.

cross section. Adding a small electromagnetic component of 5.3 mb (see next section) results in a theoretical cross section of 35.1 mb. From the ratio of experimental to theoretical cross section, a spectroscopic factor $C^2S = 0.77(4)$ is obtained, which is in good agreement with the shell-model prediction of Brown *et al.* [7, 25] of 0.74, and also with the semi-exclusive knockout experiment at lower energy (60 MeV/nucleon) [7]. In Ref. [7] a one-neutron removal cross section of 203(31) mb was measured, which includes both knockout and diffraction processes which are predicted to have similar magnitude at these beam energies. By comparison with the Eikonal calculation of Ref. [7] this yields a spectroscopic factor of 0.87(13). It was shown, however, by Esbensen and Bertsch [51] that the Eikonal approximation underestimates the cross sections at low beam energies. At 60 MeV/nucleon the ratio of the cross sections calculated in the Eikonal model and the full dynamical calculation is $\approx 0.9$ [51]. Taking this correction into account, a spectroscopic factor of 0.79(12) would be obtained. A consistent result of 0.77(12) is obtained if the coupled discretized continuum channels calculation of Tostevin *et al.* [52] is adopted for the diffraction cross section (115 mb), and the correction to the Eikonal calculation is applied for the knockout cross section only. This result compares to 0.77(4) we have obtained from the diffraction (plus small electromagnetic) cross section at 520 MeV/u. Note, that at this high energy, the difference between the Eikonal calculation and the fully dynamical calculations of Ref. [51] amounts to less than 1%.

For the $2^+$ contribution, a ratio of experimental to calculated diffraction cross section of 0.33(9) is obtained, which is rather large compared to that expected from the shell-model prediction of 0.18 [25], but in good agreement with the lower limit of 30% for the excited-state admixture obtained from the transfer reaction by Winfield *et al.* [21]. Two facts, however, prevent a precise deduction of the spectroscopic factor in this case: firstly, the feeding of the $2^+$ level by the higher-lying $1^-$ state results in the rather large error of 27% for the extracted direct feeding contribution. And secondly, dynamical excitations might be non-negligible in this very special case. This is due the fact that the cross section for the population of the $2^+$ state compared to the $0^+$ state is very small (less than 10%). A small contribution of inelastic excitation of the $2^+$ state during removal of the $s_{1/2}$ neutron might thus already contribute significantly to the cross section, as pointed out in Ref. [7]. The experimental results are summarized in Table I for the different core states populated. One recognizes that the observed cross sections for the higher-lying ($1^-$,$2^-$) states are somewhat lower than expected from theory. The $1^-$ and $2^-$ states have a $p_{3/2}$ hole structure and are thus populated by the removal of a $p$ neutron from the core, while the $2s_{1/2}$ halo neutron has to survive this reaction as a spectator, which was, however, not taken into account in the calculation. The observed reduction of about 50% might partly be related to this effect.

### C. Coulomb breakup

The large cross sections observed for the electromagnetic dissociation of halo nuclei can be explained by non-resonant transitions to the continuum due to a large overlap between the tail of the neutron wave function and continuum wave functions with large wavelength, i.e. small relative momenta $q$ (direct-breakup model). Since the effective charge $Z_{eff} \sim A^{-\lambda}$ (with $\lambda$ being the multipolarity) gets smaller for higher multipolarities, the breakup process is dominated by dipole transitions. Typel and Baur [40] estimated the $E2$ contribution for the Coulomb breakup of $^{19}$C, for instance, to be more than three orders of magnitude smaller than the $E1$ cross section. Quadrupole and higher multipolarities can thus safely be neglected and the differential cross section can be factorized into the number $N_{E1}(E^*)$ of equivalent dipole photons with energy $E^*$ associated with the rapidly varying Coulomb field of the target, and

the square of the dipole matrix elements [15, 53]:

$$\frac{d\sigma}{dE^*}(I^\pi) = (\frac{16\pi^3}{9\hbar c})N_{E1}(E^*)\sum_{nlj} CS^2(I_c^\pi, nlj) \times \sum_m |\langle \boldsymbol{q}|(Ze/A)rY_m^1|\psi_{nlj}(\boldsymbol{r})\rangle|^2. \quad (6)$$

$N_{E1}(E^*)$ is calculated using the semiclassical approximation [31] with a minimum impact parameter of $b_{\min} = 10.38$ fm as obtained from the parametrization of Ref. [54]. The influence of this particular choice for $b_{\min}$ is not important and was verified by a calculation making use of the Eikonal approach avoiding this parameter, as will be discussed later (see also the calculated probability for Coulomb breakup as a function of the impact parameter $b$, shown as solid curve in Figure 5). Similar to the Eikonal calculation for the nuclear cross sections, the Coulomb breakup cross sections are calculated for individual ground-state single-particle configurations of the neutron with a relative-motion wave function $\psi_{nlj}(\boldsymbol{r})$ and corresponding core state ($I_c^\pi$). In general, more than one configuration can contribute, and the cross section involving the core state ($I_c^\pi$) is calculated by summing over the respective configurations. In that case, the differential cross section might be used to disentangle the different contributing $l$ values [19]. The associated spectroscopic factors $CS^2(I_c^\pi, nlj)$ are obtained experimentally by the ratio of the measured partial cross sections for the population of core states ($I_c^\pi$) obtained from the gamma coincidences, and the theoretical cross section with unity spectroscopic factor. The final state $|\boldsymbol{q}\rangle$ in the continuum might be approximated by a plane wave [55, 56]. We consider, however, also the final-state interaction between the neutron and the core by taking into account an appropriate optical potential with parameters taken from the literature [57].

In Figure 4, the experimental differential cross section $d\sigma/dE^*$ populating the $^{10}$Be core in its $0^+$ ground state is compared to the result of the direct-breakup model given by equation 6. The plane-wave approximation was considered with a single-particle wave function calculated for a Woods-Saxon potential with radius $r_0 = 1.25$ and diffuseness $a = 0.7$. Prior to comparison of the theoretical cross sections for electromagnetic breakup with the measured cross section for lead target, one has to take into account the cross section for nuclear-induced breakup. This is accounted for by subtracting a properly scaled cross section measured with the carbon target, which represents the nuclear breakup; its small electromagnetic contribution (see Table I) is taken into account, however, when subtracting the scaled cross section. Since the theoretical cross section calculated in Eikonal approximation is in very good agreement with the measurement for the carbon target (see above), we assume that the ratio of cross sections for lead and carbon targets as derived from the same calculation is reliable as well, and thus derive a scaling factor of 5.4. An independent check of this ratio can be obtained from the experiment since the shape of the cross sections for nuclear and electromagnetic-induced breakup are rather different, see Figure 4: the solid curve in Figure 4 shows the sum of the measured distribution for the carbon target and the electromagnetic part as calculated by equation 6, while the individual normalization of the two contributions was obtained by a fit to the experimental data. The scaling factor obtained from this fit depends only slightly on whether the electromagnetic part is computed in plane-wave or distorted-wave approximation and results in a value of 5.0(4) or 5.6(4), respectively. In any case, the value is in very good agreement with the one derived from the Eikonal calculation. This gives further confidence in the procedure and the calculated factor of 5.4 is used in the following analysis of the Coulomb breakup cross sections. It is interesting to note, however, that this scaling factor is significantly larger than expected from a frequently used procedure of scaling the cross sections with the radius, which is suggested by a geometrical picture for peripheral reactions. This effect is especially pronounced for halo-like systems, and is less important for well bound nucleons, as can be seen from Table I by comparing the two cross sections for the lead and carbon target calculated for the removal of a $p$ neutron yielding the $1^-$ and $2^-$ excited states of $^{10}$Be.

After subtracting the nuclear contribution from the measured cross section with the lead target, the dipole strength distribution is derived from the resulting differential cross section for electromagnetic excitation by dividing out the number of equivalent photons. The experimental dipole-strength function for transitions to the $^{10}$Be ground state (solid symbols) is compared to the strength distribution as extracted from a measurement at lower beam energy by Nakamura *et al.* [12] (open symbols) in Figure 6. The shapes of the two distributions are in agreement, the absolute strength, however, differs significantly. This finding might partly be related to the fact that contributions from excited states were not subtracted in the older semi-exclusive measurement. Also higher-order effects and nuclear-electromagnetic interference might play a role at the lower beam energy of 72 MeV/nucleon [58–61], while such effects are found to be negligibly small at higher beam energies (see e.g. References [59, 60]). The continuum dipole strength integrated from the neutron threshold up to an excitation energy of 6.1 MeV amounts to 0.90(6) $e^2$fm$^2$, much larger than the dipole strength of 0.100(15) $e^2$fm$^2$ [62] observed for the transition to the first and only bound excited state in $^{11}$Be, which represents one of the strongest E1 transitions in nuclei [62–64]. The value of 0.90(6) $e^2$fm$^2$ corresponds to 4.4% of the classical Thomas-Reiche-Kuhn sum rule for dipole transitions [65]. For an integration limit of 4 MeV in relative energy, a value of 0.83(6) $e^2$fm$^2$ is obtained compared to 1.3(0.3) $e^2$fm$^2$ obtained by Nakamura *et al.* [12].

The result of the calculations with the direct-breakup model (equation 6) is displayed in Fig. 6 by the dashed and solid curves, before and after convoluting with the

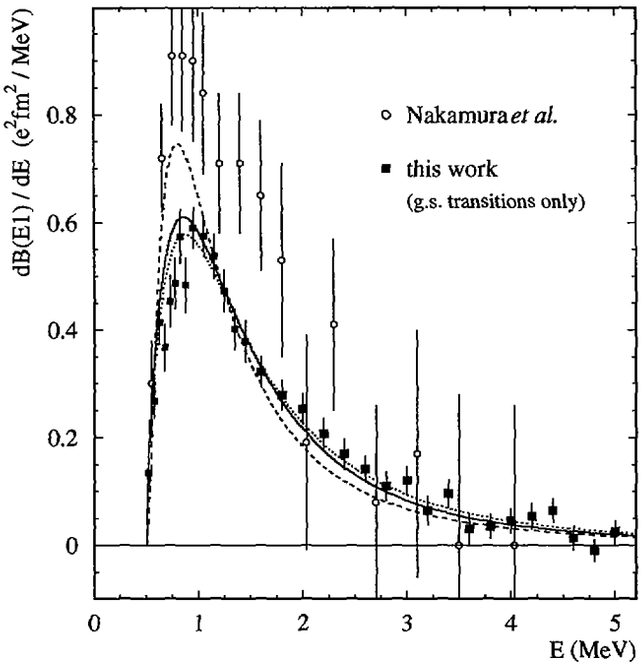


FIG. 6: Dipole-strength distribution of $^{11}$Be deduced from the measurement of the differential cross section $d\sigma/dE^*$ for electromagnetic breakup yielding the $^{10}$Be fragment in its ground state (filled symbols). The open symbols display the result obtained by Nakamura *et al.* [14] from a Coulomb-breakup experiment at lower beam energies. In the latter case, excited state contributions were not subtracted. The dashed and solid curves display the result of the direct-breakup model before and after convoluting with the instrumental response, respectively, and after multiplying with a spectroscopic factor of 0.61. The dotted curve results from a calculation using the plane-wave approximation.

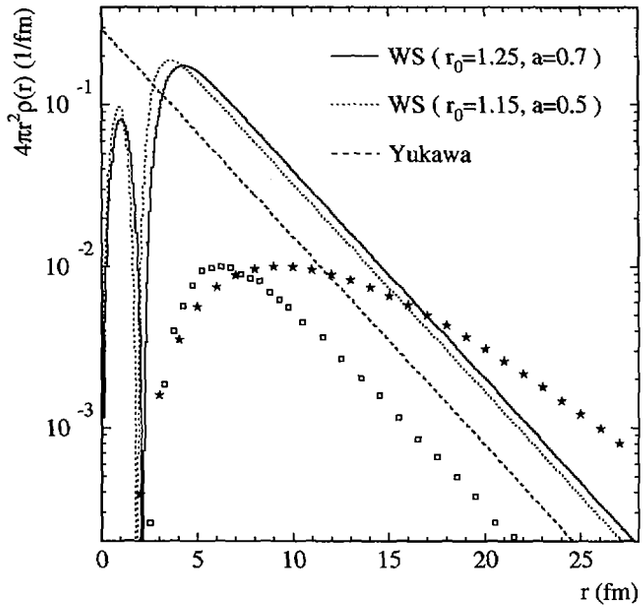


FIG. 7: Density distributions of the $2s_{1/2}$ halo neutron as a function of the neutron-core relative distance, calculated for two Woods-Saxon geometries (solid and dotted curves) and the Yukawa wave function (dashed line). The open squares and stars indicate the region of the density distribution contributing to the breakup reaction induced by nuclear diffraction or Coulomb breakup, respectively. The two breakup probabilities are given in arbitrary units.

experimental response, respectively. The distorted continuum waves were calculated with an optical potential adopting parameters from Ref. [57]. The normalization of the theoretical curve was adjusted by multiplying with a spectroscopic factor of 0.61(5) as derived from the ratio of experimental to calculated cross section for electromagnetic breakup (see Table I). First, we note a remarkable agreement of theory and experiment concerning the shape. Only minor differences can be observed in the peak region. The shape is not very sensitive to the optical potential used, as can be seen by comparison with the result for plane waves (dotted curve). The absolute strength, however, changes significantly resulting in a smaller spectroscopic factor of 0.54 for the plane-wave approximation. In order to check the sensitivity to the parameters of the optical potential, we calculated cross sections also with other choices taken from the work of Chadwick and Young [57] and Bonaccorso and Carstoiu [66], resulting in spectroscopic factors of 0.59 and 0.63, respectively. This small dependence on the parameters used is incorporated in the error for the deduced spectroscopic factor of 0.61(5) for the halo neutron in the $2s_{1/2}$ orbital coupled to the $0^+$ ground state of the $^{10}$Be core.

The calculated cross section and consequently the extracted spectroscopic factor depends to a certain extent on the parameters defining the geometry of the Woods-Saxon potential. Changing the radius parameter $r_0$ and diffuseness $a$ from $r_0 = 1.25$ and $a = 0.7$ to $r_0 = 1.15$ and $a = 0.5$, respectively, will change the asymptotic normalization of the single-particle wave function (see Figure 7) and thus its rms radius. Since the Coulomb breakup cross section is mainly sensitive to the tail of the wave function, the spectroscopic factor changes accordingly, e.g. from 0.61(5) to 0.74(6) for the $2s_{1/2}$ halo state. The stars in Figure 7 display the transition probability (for the $2s_{1/2}$ neutron) to the continuum as a function of the relative neutron-core distance. As is evident from Figure 7, the Coulomb breakup probes only the asymptotic part of the $2s_{1/2}$ ground-state wave function which does not depend on the exact geometry of the nuclear potential (apart from the normalization). This is further illustrated by comparing to a Yukawa wave function

$$\phi(r >> r_0) = N_0 \times \sqrt{2}/\rho \, \exp(-r\rho)/r, \qquad (7)$$

with $\rho = \hbar/\sqrt{2\mu B_n}$, and $\mu$ being the reduced mass, which is determined solely by the neutron separation energy $B_n$. The calculation using this wave function (dashed line in Figure 7) yields the same shape of the dipole-strength distribution. Consequently, the Coulomb breakup probes

the neutron density at around 10 fm, the value of which we give as the normalization factor $N_0 = 1.2(1)$ for the Yukawa wave function (equation 7). The corresponding rms radius of the $2s_{1/2}$ halo wave function, which is as well independent of the choice of the potential geometry, amounts to $\langle r^2\rangle^{1/2} = 5.7(4)$ fm. Both the value for the asymptotic normalization as well as the rms radius are extracted from a calculation including final-state interaction. The small uncertainties due to the choice of the optical potential parameters, as discussed above, are incorporated in the errors.

For the excited states $2^+$, $1^-$ and $2^-$, integrated cross-sections for the lead target and the electromagnetic contributions are summarized in Table I. It is observed that even high-lying states around 6 MeV are populated in the Coulomb breakup process with cross sections comparable to the nuclear dissociation. The limited statistics, however, prevents the extraction of precise spectroscopic factors for the excited states. Also, we observe a larger sensitivity to the parameters of the optical potential used in the calculation, as compared to the case of the $2s_{1/2}$ halo state.

### D. Summary and discussion

In summary, values for the asymptotic normalization and the rms radius of the neutron-relative wave function for the $2s_{1/2} \otimes^{10}$ Be($0^+$) single-particle configuration of $N_0 = 1.2(1)$ and $\langle r^2\rangle^{1/2} = 5.7(4)$ fm were derived from the differential Coulomb breakup cross section, respectively. The spectroscopic factors for this configuration deduced from the diffractive nuclear scattering cross section and from the Coulomb breakup cross section are compared in Figure 8 with those obtained from other experiments, and with two model predictions. In case of the semi-exclusive measurement of the one-neutron removal reaction at lower incident energy (60 MeV/nucleon), two values are given obtained from the Eikonal calculation (open square) [7] and for the corrected Eikonal calculation [51], see also section III B. The spectroscopic factors obtained from the nuclear cross sections measured at different beam energies (filled square and triangle) are in very good agreement, while the one derived from the electromagnetic breakup (filled circle) is about 20% smaller. Since the two measurements are complementary and have different systematic uncertainties, one may take this as an indication that the derived spectroscopic factors are certain on an absolute scale, i.e. can be interpreted as absolute single-particle occupancies within a 20% uncertainty. The results deduced from $^{10}$Be(d,p)$^{11}$Be and $^{11}$Be(p,d)$^{10}$Be transfer reaction experiments are indicated by the open circles [23] and star [21], respectively. The three circles display the result of different theoretical analysis within the framework of distorted-wave Born approximation yielding spectroscopic factors of 0.77 [23] and 0.60 [22], and 0.36 [22], the latter one from a more elaborated reaction model including excitation and breakup [22]. The uncertainty due to the choice of parameters for the optical potential of the value 0.66 (star) deduced from the inverse reaction is indicated by the dash-dotted error bar (see Figures 7 and 8 of Ref. [21]). The results of both transfer reactions are within their uncertainties in agreement with both values obtained from the nuclear and the Coulomb breakup reactions, respectively. The lower value of 0.36, however, is clearly in disagreement with the breakup data and can be discarded, although the underlying analysis used a rather elaborated reaction theory. Within the apparent uncertainties of experimentally deduced spectroscopic factors, both theoretical models of Brown *et al.* [25] and Otsuka *et al.* [67] indicated by the solid and dotted lines in Figure 8, respectively, are in agreement with experiment. Note, however, that no center-of-mass correction was applied to the shell-model values as proposed, e.g., in Refs. [68–70]. Applying the corresponding factor of $A^2/(A-1)^2 = (11/10)^2$ would yield a ratio $S_{exp}/S_{SM}$ of 0.86 and 0.68 compared to the value of Brown *et al.* [7, 25] for the two spectroscopic factors extracted from nuclear and Coulomb dissociation, respectively. We now turn back to the observed discrepancy of 20% between the nuclear and Coulomb breakup data, and discuss in the following possible systematic uncertainties, which might explain the observed difference.

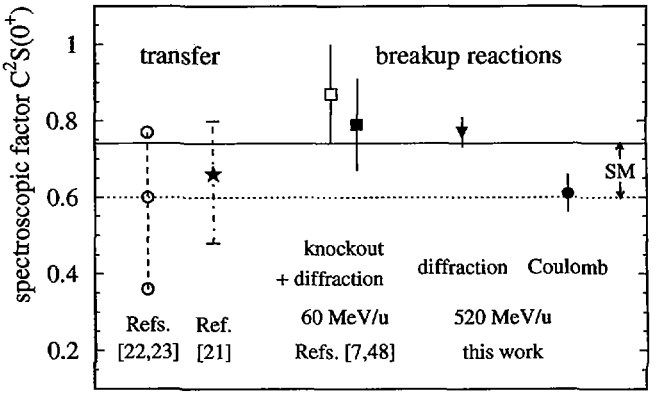


FIG. 8: Spectroscopic factors for the $2s_{1/2} \otimes^{10}$ Be($0^+$) halo state derived from different reactions. The open circles connected by the dashed line indicate the values obtained from different analysis [22, 23] of the $^{10}$Be(d,p)$^{11}$Be transfer reaction [23], while the star displays the result deduced from the inverse $^{11}$Be(p,d)$^{10}$Be reaction using a 35.3 MeV/nucleon $^{11}$Be secondary beam [21]. The open square marks the result derived from the cross section and Eikonal calculation of Ref. [7], while the filled square displays the corresponding value after correction of the Eikonal value according to Ref. [51] (see text). The results deduced from diffractive and electromagnetic breakup (this work) are shown by the filled triangle and circle, respectively. The two lines indicate the predictions of the shell model by Brown *et al.* [25] (solid line) and the variational shell model by Otsuka *et al.* [67] (dotted line).

As discussed in several publications, second order ef-

fects and nuclear-electromagnetic interference effects can be neglected in case of high-energy electromagnetic excitation (see e.g. Refs. [59, 60]). The influence of the choice of parameters for the optical potential needed to account for the final-state interactions is rather small, as discussed above, and is already included in the error of the deduced spectroscopic factor of 0.61(5). Remaining inputs to the calculation are the bound-state wave function, which is a common input for both, nuclear and electromagnetic excitations, and the minimum impact parameter $b_{\rm min}$ in the semi-classical calculation of the Coulomb breakup cross section. Since $^{11}$Be is a halo nucleus, the choice of this lower integration cutoff is not obvious, and a value corresponding to the systematics [54] derived from stable nuclei might fail. Therefore, we performed, in addition, a calculation using the 'soft-spheres' model [71], which avoids this parameter. Here, the nuclear absorption is properly taken into account by calculating the reaction probability within the Eikonal model. The resulting nuclear reaction probability for 520 MeV/nucleon $^{11}$Be + Pb is shown in Figure 5 by the dashed curve. The same densities were used as for the calculation of the nuclear one-neutron removal cross sections. Multiplying the Coulomb excitation probability with the corresponding survival probability (no nuclear reaction) yields the solid curve. The result for the integrated cross section for electromagnetic dissociation is very close to the result we have obtained with a sharp cut-off of $b_{\rm min}$ = 10.38 fm, which is given by the parametrization of Benesh *et al.* [54] (including a small correction for Coulomb deflection [30]). A similar conclusion was obtained for the electromagnetic excitation of the giant dipole resonance in stable nuclei in Ref. [33]. Thus, the halo does not play an important role for the choice of the minimum impact parameter. This can be understood by inspecting the reaction probabilities as shown in Figure 5: the nuclear reaction probability (dashed curve in Figure 5) is rather small (< 10%) in the region where the low-density tail of the halo wave function dominates, as can be seen by comparing the dashed curve with the nuclear one-neutron removal probability (dash-dotted curve). It is also interesting to note that only a small part of the one-neutron Coulomb breakup cross section results from the region of impact parameters where nuclear and electromagnetic processes compete: only 10% of the cross section is reached by integrating the electromagnetic cross section over impact parameter up to $b$ = 13 fm (see dotted curve); at this impact parameter, the probability for nuclear one-neutron removal is already down by a factor of two. This sets an upper limit on possible interference effects, independent from the observation of many reaction-theory calculations indicating that such effects are negligible at high beam energy, and in particular for angle-integrated observables. In concluding this paragraph, we note that the systematic uncertainties in calculating the Coulomb breakup cross section discussed above seem to be small and cannot explain the observed 20% discrepancy between the two spectroscopic factors deduced.

We now turn to possible systematic uncertainties in calculating the nuclear cross section. From the fact that the two spectroscopic factors deduced from the measurement of the diffraction plus knockout cross section at lower incident energy and the diffraction cross section at 520 MeV/nucleon are in very good agreement, we conclude that the energy-dependence of the cross section as well as the differentiation between the two reaction mechanisms, knockout and diffraction, is well under control (within the 15% error given for the experimental result of [7]). One important ingredient to the Eikonal calculation is the core-target profile function, which takes into account reactions between the core and the target leading to reaction channels other than the one selected experimentally, namely the $^{10}$Be core in the final channel. To calculate this quantity, a density distribution of the core is assumed which reproduces the reaction cross section of the free $^{10}$Be nucleus with the target. A slight modification of this density distribution might result in a sizable change of the one-neutron removal cross section, as pointed out, e.g., by Esbensen and Bertsch [51]. A reduction of the rms radius of the $^{10}$Be core density by 10% (keeping the harmonic oscillator density distribution), however, increases the one-neutron removal cross section only by about 5%. The uncertainty of calculating absolute cross sections due to ambiguities in the core-target profile function are thus rather small, at least for halo-like wave functions as in the present case, and are not likely to explain the observed difference in the spectroscopic factors.

A last possible uncertainty that we like to address, is the parameter dependence in the calculation of the bound-state wave function, which is used as an input in both calculations. The two reactions, nuclear and electromagnetically induced neutron removal, sample different parts of this wave function. This is illustrated in Figure 7, where the regions of sensitivity are indicated for the nuclear (squares) and electromagnetically (stars) induced reactions, respectively. The nuclear reaction probes the wave function at the surface close to the core (close to the binding potential). In fact, the reaction is not sensitive to the inner part of the neutron wave function, which is 'shadowed' by the core. For the electromagnetically induced breakup, the transition probability is largest at about a distance of 10 fm from the core (see stars in Figure 7). Here, the sensitivity to the inner part is reduced due to the nature of the dipole-transition operator weighting the single-particle density with the relative distance $r$ (see equation 6), thus avoiding the complication inherent in calculating core absorption. As a consequence of this different sensitivity, a change, e.g., of the geometry of the bound-state potential might not yield the same change in the calculated cross sections. As an example, we calculate the cross sections for a different parameter set for the Woods-Saxon potential with $a$ = 0.5 and $r_0$ = 1.15 yielding a wave function with 17% smaller asymptotic density (see Figure 7). The cross sec-

tions, and thus spectroscopic factors, change by 13% and 18% for the nuclear and Coulomb breakup, respectively. Such an effect would consequently reduce the discrepancy from 20% to about 15%, again too small to explain the difference between the two deduced values for the single-particle occupancy.

In summarizing this subsection, we note that several possible uncertainties in the theoretical estimation of nuclear and electromagnetic one-neutron removal cross sections which are discussed quantitatively above, turn out to be rather small, and are consequently not suitable to explain the observed difference of 20% for the deduced spectroscopic factors. The discrepancy may reflect the limitations of the single-particle models used. In order to understand this effect quantitatively, theoretical investigations concerning reaction theory are called for, but also a systematic investigation and comparison of deduced single-particle occupancies derived from nuclear and electromagnetically induced breakup reactions is needed.

## IV. CONCLUSION

By using a secondary beam of $^{11}$Be produced in a fragmentation reaction, we have investigated the nuclear and electromagnetic inelastic scattering into the continuum by an exclusive measurement of all decay products, i.e. a coincident measurement of the neutron, the $^{10}$Be core and the gamma rays from excited core states. Differential and integrated cross sections were derived for diffraction dissociation and Coulomb breakup, differentiated according to the core states populated. The dominant contribution to the cross sections is found to originate from transitions of the neutron in the $2s_{1/2}$ state, populating the $^{10}$Be core in its ground state. Small contributions from the $1d_{5/2} \otimes^{10}$ Be$(2^+)$ configuration, as well as removal from more deeply bound states yielding excited core states were also observed. Quantitative results for the $E1$ continuum strength distribution associated solely with the halo $2s_{1/2}$ neutron could be derived for the first time. From the dipole-strength distribution, the spectroscopic factor for the $2s_{1/2} \otimes^{10}$Be$(0^+)$ configuration was deduced as well as the asymptotic normalization and the root-mean-square radius of the core-neutron relative-motion wave function. The spectroscopic factor deduced from the diffraction dissociation cross section is in good agreement with a measurement of the neutron removal at lower incident energy. A completely independent extraction of this quantity from the dipole strength yields an occupancy about 20% smaller than the one derived from the nuclear processes. Possible reasons were discussed quantitatively and found to be too small to account for the observed difference. This difference thus remains to be understood and might reflect the systematic uncertainties inherent in the methods and models used. The very large dipole-transition probability observed close to the particle-separation threshold is a direct consequence of the halo character of the neutron wave function. The consequently large cross sections in conjunction with the enormous sensitivity to the tail of the wave function makes Coulomb dissociation a promising and very efficient spectroscopic method to extract quantitative structure information on the ground-state configuration of weakly bound nuclei, if available as secondary beams even of very low intensity.

### Acknowledgments

We are grateful to C.A. Bertulani and S. Typel for many useful discussions. This work was supported by the German Federal Minister for Education and Research (BMBF) under Contracts 06 OF 933, 06 MZ 963I, and 06 DA 915I, and by GSI via Hochschulzusammenarbeitsvereinbarungen under Contracts OFELZK, MZKRAK, and partly supported by the Polish Committee of Scientific Research under Contract No. 2PB03 144 18. Support was received in part by DAAD/CAPES cooperative agreement no. 415-bra-probral/bu.

[1] A collection of recent review articles can be found in the *Special Issue on Research Opportunities with Accelerated Beams of Radioactive Ions*, edited by I. Tanihata, Nucl. Phys. A **693** (2001).

[2] I. Tanihata, H. Hamagaki, O. Hashimoto, Y. Shida, N. Yoshikawa, K. Sugimoto, O. Yamakawa, T. Kobayashi, N. Takahashi, Phys. Rev. Lett. **55** (1985) 2676;

[3] I. Tanihata, T. Kobayashi, O. Yamakawa, S. Shimoura, K. Ekuni, K. Sugimoto, N. Takahashi, T. Shimoda, and H. Sato, Phys. Lett. B **206** (1988) 592.

[4] P.G. Hansen, B. Jonson, Europhys. Lett. **4** (1987) 409.

[5] P.G. Hansen, A.S. Jensen, B. Jonson, Annu. Rev. Nucl. Part. Sci. **45** (1995) 591.

[6] P.G. Hansen, B.M. Sherrill, Nucl. Phys. A **693** (2001) 133.

[7] T. Aumann, A. Navin, D.P. Balamuth, D. Bazin, B. Blank, B.A. Brown, J.E. Bush, J.A. Caggiano, B. Davids, T. Glasmacher, V. Guimarães, P.G. Hansen, R.W. Ibbotson, D. Karnes, J.J. Kolata, V. Maddalena, B. Pritychenko, H. Scheit, B.M. Sherrill, J.A. Tostevin, Phys. Rev. Lett. **84** (2000) 35.

[8] T. Aumann, D. Aleksandrov, L. Axelsson, T. Baumann, M.J.G. Borge, L.V. Chulkov, J. Cub, W. Dostal, B. Eberlein, Th.W. Elze, H. Emling, H. Geissel, V.Z. Goldberg, M. Golovkov, A. Grünschloß, M. Hellström, K. Hencken, J. Holeczek, R. Holzmann, B. Jonson, A.A. Korshenninikov, J.V. Kratz, G. Kraus, R. Kulessa, Y. Leifels, A. Leistenschneider, T. Leth, I. Mukha, G. Münzenberg, F. Nickel, T. Nilsson, G. Nyman, B. Petersen, M. Pfützner, A. Richter, K. Riisager, C. Scheidenberger, G. Schrieder, W. Schwab, H. Simon, M.H. Smedberg, M. Steiner, J. Stroth, A. Surowiec, T. Suzuki, O. Tengblad, M.V.

Zhukov, Phys. Rev. C **59** (1999) 1152.
[9] D. Sackett, K. Ieki, A. Galonsky, C.A. Bertulani, H. Esbensen, J.J. Kruse, W.G. Lynch, D.J. Morrissey, B.M. Sherrill, H. Schulz, A. Sustich, J.A. Winger, F. Deák, Á. Horváth, Á. Kiss, Z. Seres, J.J. Kolata, R.E. Warner, D. Humphrey, Phys. Rev. C **48** (1993) 118.
[10] S. Shimoura, T. Nakamoura, M. Ishihara, N. Inabe, T. Kobayashi, T. Kubo, R.H. Siemssen, I. Tanihata, Y. Watanabe, Phys. Lett B **348** (1995) 29.
[11] M. Zinser, F. Humbert, T. Nilsson, W. Schwab, H. Simon, T. Aumann, M. Borge, L.V. Chulkov, J. Cub, Th.W. Elze, H. Emling, H. Geissel, D. Guillemaud-Mueller, P.G. Hansen, R. Holzmann, H. Irnich, B. Jonson, J.V. Kratz, R. Kulessa, Y. Leifels, A. Magel, A.C. Mueller, G.Münzenberg, F. Nickel, G. Nyman, A. Richter, K. Riisager, C. Scheidenberger, G. Schrieder, K. Stelzer, J.Stroth, A. Surowiec, O. Tengblad, E. Wajda and E. Zude, Nucl. Phys. A **619** (1997) 151.
[12] T. Nakamura, S. Shimoura, T. Kobayashi, T. Teranishi, K. Abe, N. Aoi, Y. Doki, M. Fujimaki, N. Inabe, N. Iwasa, K. Katori, T. Kubo, H. Okuno, T. Suzuki, I. Tanihata, Y. Watanabe, A. Yoshida, M. Ishihara, Phys. Lett. B **331** (1994) 296.
[13] R. Anne, R. Bimbot, S. Dogny, H. Emling, D. Guillemaud-Mueller, P.G. Hansen, P. Hornshøj, F. Humbert, B. Jonson, M. Keim, M. Lewitowicz, P. Møller, A.C. Mueller, R. Neugart, T. Nilsson, G. Nyman, F. Pougheon, K. Riisager, M.-G. Saint-Laurent, G. Schrieder, O. Sorlin, O. Tengblad, K. Wilhelmsen Rolander, Nucl. Phys. A **575** (1994) 125.
[14] T. Nakamura, N. Fukuda, T. Kobayashi, N. Aoi, H. Iwasaki, T. Kubo, A. Mengoni, M. Notani, H. Otsu, H. Sakurai, S. Shimoura, T. Teranishi, Y.X. Watanabe, K. Yoneda, M. Ishihara, Phys. Rev. Lett. **83** (1999) 1112.
[15] G. Baur and C.A. Bertulani, Nucl. Phys. A **480** (1988) 615.
[16] C. A. Bertulani, L.F. Canto, and M.S. Hussein, Phys. Rep. **6** (1993) 281.
[17] C.A. Bertulani, M.S. Hussein, and G. Münzenberg, *Physics of radioactive Beams*, ISBN 1-59033-141-9, Nova Science Publishers Inc, New York (2001), chapter 7.
[18] F. Catara, C.H. Dasso, A. Vitturi, Nucl. Phys. A **602** (1996) 181.
[19] U. Datta Pramanik, T. Aumann, K. Boretzky, B.V. Carlson, D. Cortina, Th.W. Elze, H. Emling, H. Geissel, A. Grünschloss, M. Hellström, S. Ilievski, J.V. Kratz, R. Kulessa, Y. Leifels, A. Leistenschneider, E. Lubkiewicz, G. Münzenberg, P. Reiter, H. Simon, K. Sümmerer, E. Wajda, W. Walus, Phys. Lett. B. **551** (2003) 63.
[20] S. Fortier, S. Pita, J.S. Winfield, W.N. Catford, N.A. Orr, J. Van de Wiele, Y. Blumenfeld, R. Chapman, S.P.G. Chappell, N.M. Clarke, N. Curtis, M. Freer, S. Galès, K.L. Jones, H. Langevin-Joliot, H. Laurent, I. Lhenry, J.M. Maison, P. Roussel-Chomaz, M. Shawcross, M. Smith, K. Spohr, T. Suomijärvi, A. de Vismes, Phys. Lett. B **461** (1999) 22.
[21] J.S. Winfield, S. Fortier, W.N. Catford, S. Pita, N.A. Orr, J. Van de Wiele, Y. Blumenfeld, R. Chapman, S.P.G. Chappell, N.M. Clarke, N. Curtis, M. Freer, S. Galès, H. Langevin-Joliot, H. Laurent, I. Lhenry, J.M. Maison, P. Roussel-Chomaz, M. Shawcross, K. Spohr, T. Suomijärvi, A. de Vismes, Nucl. Phys. A **683** (2001) 48.
[22] N.K. Timofeyuk and R.C. Johnson, Phys. Rev. C **59** (1999) 1545.
[23] B. Zwieglinki, W. Benenson, R.G.H. Robertson, and W.R. Coker, Nucl. Phys. A **315** (1979) 124.
[24] E.K. Warburton and B.A. Brown, Phys. Rev. C **46** (1992) 923.
[25] B.A. Brown, Progr. in Part. and Nucl. Phys. **47** (2001) 517.
[26] H. Simon, D. Aleksandrov, T. Aumann, L. Axelsson, T. Baumann, M.J.G. Borge, L.V. Chulkov, R. Collatz, J. Cub, W. Dostal, B. Eberlein, Th.W. Elze, H. Emling, H. Geissel, A. Grünschloß, M. Hellström, J. Holeczek, R. Holzmann, B. Jonson, J.V. Kratz, G. Kraus, R. Kulessa, Y. Leifels, A. Leistenschneider, T. Leth, I. Mukha, G. Münzenberg, F. Nickel, T. Nilsson, G. Nyman, B. Petersen, M. Pfützner, A. Richter, K. Riisager, C. Scheidenberger, G. Schrieder, W. Schwab, M.H. Smedberg, J. Stroth, A. Surowiec, O. Tengblad, and M.V. Zhukov, Phys. Rev. Lett. **83** (1999) 496.
[27] A. Navin, D.W. Anthony, T. Aumann, T. Baumann, D. Bazin, Y. Blumenfeld, B.A. Brown, T. Glasmacher, P.G. Hansen, R.W. Ibbotson, P.A. Lofy, V. Maddalena, K. Miller, T. Nakamura, B. Pritychenko, B.M. Sherrill, E. Spears, M. Steiner, J.A. Tostevin J. Yurkon, and A. Wagner, Phys. Rev. Lett. **85** (2000) 266.
[28] H. Sagawa, B.A. Brown, and H. Esbensen, Phys. Lett. B **309** (1993) 1.
[29] N. Michel, W. Nazarewicz, M. Ploszajczak, and J. Okolowicz, Phys. Rev. C **67** (2003) 054311.
[30] A. Winther and K. Alder, Nucl. Phys. A **319** (1979) 518.
[31] C.A. Bertulani and G. Baur, Phys. Rep. **163** (1988) 299.
[32] G. Baur, K. Hencken, and D. Trautmann, nucl-th/0304041 (2003)
[33] T. Aumann, P.F. Bortignon, and H. Emling, Annu. Rev. Nucl. Part. Sci. **48** (1998) 351.
[34] H. Geissel, P. Armbruster, K.H. Behr, A. Brünle, K. Burkard, M. Chen, H. Folger, B. Franczak, H. Keller, O. Klepper, B. Langenbeck, F. Nickel, E. Pfeng, M. Pfützner, E. Roeckl, K. Rykaczewski, I. Schall, D. Schardt, C. Scheidenberger, K.-H. Schmidt, A. Schröter, T. Schwab, K. Sümmerer, M. Weber, G. Münzenberg, T. Brohm, H.-G. Clerc, M. Fauerbach, J.-J. Gaimard, A. Grewe, E. Hanelt, B. Knödler, M. Steiner, B. Voss, J. Weckenmann, C. Ziegler, A. Magel, H. Wollnik, J.P. Dufour, Y. Fujita, D.J. Vieira, B. Sherrill, Nucl. Instr. and Meth. B **70** (1992) 286.
[35] A. Leistenschneider, T. Aumann, K. Boretzky, D. Cortina, J. Cub, U.D. Pramanik, W. Dostal, Th.W. Elze, H. Emling, H. Geissel, A. Grünschloss, M. Hellström, R. Holzmann, S. Ilievski, N. Iwasa, M. Kaspar, A. Kleinböhl, J.V. Kratz, R. Kulessa, Y. Leifels, E. Lubkiewicz, G. Münzenberg, P. Reiter, M. Rejmund, C. Scheidenberger, C. Schlegel, H. Simon, J. Stroth, K. Sümmerer, E. Wajda, W. Walús, S. Wan, Phys. Rev. Lett. **86** (2001) 5442.
[36] A. Leistenschneider, T. Aumann, K. Boretzky, L.F. Canto, B.V. Carlson, D. Cortina, U.D. Pramanik, Th.W. Elze, H. Emling, H. Geissel, A. Grünschloss, K. Helariutta, M. Hellström, M.S. Hussein, S. Ilievski, K.L. Jones, J.V. Kratz, R. Kulessa, L.H. Khiem, E. Lubkiewicz, G. Münzenberg, R. Palit, P. Reiter, C. Scheidenberger, K.-H. Schmidt, H. Simon, K. Sümmerer, E. Wajda, W. Walús, Phys. Rev. C. **65** (2002) 064607.
[37] V. Metag, D. Habs, and D. Schwalm, Comm. on Nucl. Part. Phys. **16** (1986) 213.
[38] J. Cub, G. Stengel, A. Grünschloß, K. Boretzky, T. Au-

mann, W. Dostal, B. Eberlein, Th.W. Elze, H. Emling, J. Holeczek, G. Ickert, J. Holeczek, R. Holzmann, J.V. Kratz, R. Kulessa, Y. Leifels, H. Simon, K. Stelzer, J. Stroth, A. Surowiec, E. Wajda, Nucl. Instr. and Meth. A **402** (1998) 67.

[39] T. Blaich, Th.W. Elze, H. Emling, H. Freiesleben, K. Grimm, W. Henning, R. Holzmann, G. Ickert, J.G. Keller, H. Klingler, W. Kneissl, R. Knig, R. Kulessa, J.V. Kratz, D. Lambrecht, J.S. Lange, Y. Leifels, E. Lubkiewicz, M. Proft, W. Prokopowicz, C. Schtter, R. Schmidt, H. Spies, K. Stelzer, J. Stroth, W. Walús, E. Wajda, H.J. Wollersheim, M. Zinser, E. Zude, Nucl. Instr. and Meth. A **314** (1992) 136.

[40] S. Typel and G. Baur, Phys. Rev. C **64** (2001) 024601.

[41] F. Ajzenberg-Selove, Nucl. Phys. A **490** (1999) 1.

[42] GEANT, Cern Library Long Writup W5013 (1994).

[43] K. Hencken, G. Bertsch, and H. Esbensen, Phys. Rev. C **54** (1996) 3043.

[44] G.F. Bertsch, K. Hencken, and H. Esbensen, Phys. Rev. C **57** (1998) 1366.

[45] H. de Vries, C.W. de Jager, and C. de Vries, Atomic Data and Nuclear Data Tables **36** (1987) 495.

[46] A. Ozawa, T. Suzuki, and I. Tanihata, Nucl. Phys. A **693** (2001) 32.

[47] W. Bauhoff, Atomic Data and Nuclear Data Tables **35** (1986) 429.

[48] S.K. Charagi and S.K. Gupta, Phys. Rev. C **41** (1989) 1610.

[49] L. Ray, Phys. rev. C **20** (1979) 1857.

[50] J.A. Tostevin, J. Phys. G: Nucl. Part. Phys **25** (1999) 735.

[51] H. Esbensen and G.F. Bertsch, Phys. Rev. C **64** (2001) 014608.

[52] J.A. Tostevin, D. Bazin, B.A. Brown, T. Glasmacher, P.G. Hansen, V. Maddalena, A. Navin, and B.M. Sherrill, Phys. Rev. C **66** (2002) 024607.

[53] G. Baur, C.A. Bertulani, and H. Rebel, Nucl. Phys. A **458** (1986) 188.

[54] C.J. Benesh, B.C. Cook, and J.P. Vary, Phys. Rev. C **89** (1989) 1198.

[55] T. Otsuka, M. Ishihara, N. Fukunishi, T. Nakamura, and M. Yokoyama, Phys. Rev. C **49** (1994) R2289.

[56] D. Ridikas, M.H. Smedberg, J.S. Vaagen, M.V. Zhukov, Nucl. Phys. A **628** (1998) 363.

[57] Chadwick and Young, Nucl. Sci. Eng. **123** (1996) 17.

[58] S. Typel and R. Shyam, Phys. Rev. C **64** (2001) 024605.

[59] J. Margueron, A. Bonaccorso, and D.M. Brink, Nucl. Phys. A **703** (2002) 105.

[60] P. Banerjee, G. Baur, K. Hencken, R. Shyam, and D. Trautmann, Phys. Rev. C **65** (2002) 064602.

[61] R. Chatterjee and R. Shyam, preprint nucl-th/0211042 (2002).

[62] T. Nakamura, T. Motobayashi, Y. Ando, A. Mengoni, T. Nishio, H. Sakurai, S. Shimoura, T. Teranishi, Y. Yanagisawa, M. Ishihara, Phys. Lett. B **394** (1997) 11.

[63] M. Fauerbach, M.J. Chromik, T. Glasmacher, P.G. Hansen, R.W. Ibbotson, D.J. Morrissey, H. Scheit, P. Thierolf, M. Thoennessen, Phys. Rev. C **56** (1997) R1.

[64] D.J. Millener, J.W. Olness, and E.K. Warburton, Phys. Rev. C **28** (1983) 497.

[65] A. Bohr and B.R. Mottelson, *Nuclear Structure*, Benjamin, London (1975) Vol. 2.

[66] A. Bonaccorso and F. Carstoiu, Phys. Rev. C **61** (2000) 034605.

[67] T. Otsuka, N. Fukunishi, and H. Sagawa, Phys. Rev. Lett. **70** (1993) 1385.

[68] B.A. Brown, P.G. Hansen, B.M. Sherrill, and J.A. Tostevin, Phys. Rev. C **65** (2002) 06160.

[69] A.E.L. Dieperink and T. de Forest, Phys. Rev. C **10** (1974) 543.

[70] P.G. Hansen and J.A. Tostevin, MSU-NSCL preprint MSUCL-1258, to be published in Annu. Rev. Nucl. Part. Sci. **53** (2003).

[71] T. Aumann, C.A. Bertulani, and K. Sümmerer, Phys. Rev. C **51** (1995) 416.

[72] The asymmetric response function $f(E)$ can be well approximated by the relation

$$f(E) = \sqrt{E}\exp((c-E)/b) \times \mathrm{erf}(E_x),$$

$$E_x = (c-E)/\sqrt{2}/\sigma + \sigma/\sqrt{2}/b.$$

The parameters depending on the relative energy $E_{rel}$ were determined from a fit to the simulated response:

$$c = 0.933 \times E_{rel} - 0.185,$$

$$b = 0.040 + 0.228 \times E_{rel}^{0.415},$$

$$\sigma = 0.075 + 0.239 \times E_{rel}^{0.682}.$$

The solid curves in Figure 2 display above response function for the three energies shown.